PHYSICAL REVIEW B VOLUME 26, NUMBER 12 15 DECEMBER 1982

Phonon conduction in elastically anisotropic cubic crystals

A. K. McCurdy
Electrical Engineering Department, Worcester Polytechnic Institute, Worcester, Massachusetts 01609
(Received 16 March 1981; revised manuscript received 12 February 1982)

Striking differences in the boundary-scattered phonon conductivity and effective phonon mean free path are predicted along the principal axes of cubic crystals. The results are shown to be the result of phonon focusing arising from elastic anisotropy. Normalized curves of boundary-scattered effective phonon mean free path and phonon conductivity have been calculated for samples of square cross section as a function of the elastic anisotropy, $A=2C_{44}/(C_{11}-C_{12})$, and the elastic ratio, C_{12}/C_{11}. Normalized curves of phonon specific heat and effective velocity have been calculated as a function of the same variables. The effective phonon mean free path has also been calculated as a function of the sample side-face—thermal-length ratio, D/L. Anisotropies of more than 50% are possible for different rod axes. Silicon and calcium fluoride, materials in which this anisotropy was first reported, are shown to be very favorable materials to demonstrate this anisotropy. For silicon and calcium fluoride samples of rectangular cross section the thermal conduction is shown to depend upon the crystallographic orientation and width ratio of the side faces for samples with the same ⟨110⟩ rod axis. Results are expressed in a convenient form for predicting the phonon conductivity of elastically anisotropic crystals, given the linear dimensions, the density, and the elastic constants.

I. INTRODUCTION

Thermal energy in dielectric solids is carried by phonons. At sufficiently low temperatures the phonons propagate ballistically so that in the absence of defect or impurity scattering, the mean free path becomes limited by the linear dimensions of the sample.[1–4] A theory of the thermal conductivity applicable to this temperature range was first developed by Casimir.[5] Corrections to Casimir's theory have been derived for samples of finite length,[6] and for samples in which a fraction of the phonons are specularly reflected from the end surfaces.[7] Calculations using the Casimir theory, although in qualitative agreement with experiments, nevertheless neglect the effects of elastic anisotropy upon ballistic-phonon propagation.

Heat-pulse experiments, however, have shown striking differences (up to factors of 100) in the intensity of phonons propagating ballistically in an elastically anisotropic crystal.[8,9] These results were shown to arise from phonon focusing owing to the fact that in elastically anisotropic crystals the phonon constant-energy surfaces in wave-vector space are nonspherical. The phonon phase velocity is parallel to the wave vector $\vec{k}$, but the group velocity is normal to the constant-energy surface in $\vec{k}$ space. The group velocity or direction of energy flow is therefore not, in general, parallel to the phase velocity.[10] The angular deviation between the phase and group velocity depends upon the direction of the wave vector $\vec{k}$, the phonon polarization, and the elastic anisotropy. Phonon focusing occurs whenever the direction of the group velocity varies more slowly over some small solid angle with wave-vector direction than for an elastically isotropic solid, so that an isotropic distribution of wave vectors such as that emitted by an ideal heat source gives rise to an increased density in group-velocity space. Since the energy flow is in the direction of the group velocity (i.e., normal to the constant-energy surface in $\vec{k}$ space) an enhanced energy flow occurs about any strongly focused directions.[10] The observed phonon intensities depend not only upon the propagation direction and the polarization but also upon the detector size and shape,[11] and in high-resolution experiments upon specular and diffuse phonon reflections.[12]

The thermal conductivity in the boundary-scattering region is approximately inversely proportional to the square of the phonon velocity. The slower modes, therefore, contribute most to the flow of heat. It thus follows that any strong enhancement of the thermal conductivity due to phonon focusing arises primarily from strong focusing of the slower-velocity transverse modes. The strongest phonon focusing occurs along direc-

tions where the group-velocity surface exhibits cuspidal edges or cuspidal onset.

Calculations for silicon and calcium floride showed strong focusing of transverse waves in silicon about the ⟨100⟩ axes and in all directions in {100} planes, and in calcium fluorides about the ⟨111⟩ axes and in all directions in {110} planes.[13] The strong phonon focusing in silicon is due to the presence of cuspidal edges about the ⟨100⟩ axes and very narrow cusps about the {100} planes. In calcium fluoride, with contrasting elastic anistropy, the strong focusing is due to narrow cusps around a collinear axis near the ⟨111⟩ direction in the {110} plane and wider cusps about the {110} planes. The wider cuspidal surfaces in calcium fluoride result in lower phonon intensities and smaller expected anisotropies in the thermal conductivity.

Subsequent measurements of the thermal conductivity of silicon and calcium fluoride demonstrated clearly observable anisotropies at all temperatures below the thermal-conductivity maximum.[13,14] The thermal conduction for samples of square cross section was found to depend upon the crystallographic orientation of the rod axis, the variation being as much as 50% for silicon and 40% in calcium fluoride. For silicon the thermal conductivity of ⟨100⟩ axis rods was highest, that of rods with ⟨111⟩ axis lowest. For calcium fluoride the thermal conductivity of ⟨111⟩ axis rods was highest, that of rods with ⟨100⟩ axis lowest, in contrast with silicon. For samples of rectangular cross section the thermal conduction was found to depend, in addition, upon the orientation and width ratio of the side faces, the variation being as much as 30% for silicon samples with the same ⟨110⟩ rod axis.[13] The sample having the wider-side face in the {100} plane exhibited a higher conductivity than the rod with the wider-side face in the {110} plane. All of these results were consistent with phonon-focusing calculations.

The predictions of Casimir's theory, end corrected for finite thermal length and generalized to include phonon focusing, gave quantitative agreement with experimental results without using any adjustable parameters. More recent measurements of the thermal conductivity of lithium fluoride[15] and diamond[16,17] were qualitatively consistent with those expected from phonon-focusing considerations. Similar anisotropies in the thermal conductivity have been predicted in sufficiently defect-free superconducting lead and niobium at $T/T_c \ll 1$.[18]

Phonon-focusing effects have also been studied in elastically anisotropic hexagonal,[19] tetragonal and orthorhombic,[20] and trigonal and monoclinic crystals.[21] Calculations have recently been published for diamond, germanium, and silicon,[22] aluminum oxide and α-quartz,[23] and gallium arsenide.[11,24] Effects of phonon focusing have been recently observed in heat-pulse experiments in solid ^{4}He,[25] diffuse and specular phonon-reflection experiments in Al_2O_3,[12,26] interaction of ballistic phonons in the electron-hole liquid in germanium,[27] imaging of electron-hole droplets[28,29,31] and ballistic phonons in germanium,[29–31] imaging of phonon distributions in silicon using the fountain pressure of superfluid ^{4}He films,[32] and photoexcitation experiments in GaAs and $Al_{0.5}Ga_{0.5}As$.[33]

Expressions for the phonon-focusing amplification factor were originally derived by Maris.[10] Amplification factors have also been derived for collinear directions in the hexagonal[19] and the orthorhombic lattice.[20,34] Alternative expressions suitable for numerical computation have also been given for arbitrary directions in $\vec{k}$ space. Philip *et al.*[24] have shown that the inverse phonon-amplification factor is proportional to the Jacobian of the transformation relating the polar angles of the group velocity to those for the phase velocity. An alternative expression has been given by Lax *et al.*[11] in terms of the Gaussian curvature of the energy surface, the wave vector, and the angular deviation between the phase and group velocities.

Calculations for silicon and calcium fluoride have recently been generalized to include elastically anisotropic materials of any crystal structure. Boundary-scattered thermal conductivities have been calculated for a number of materials including Al_2O_3 and α-quartz.[35] Only results for cubic crystals, however, are presented here. In Sec. II the relation between the phase- and group-velocity directions and phonon focusing is discussed for elastically anisotropic crystals. Normalized calculations of phonon specific heat, effective velocity, boundary-scattered mean free path, and phonon conductivity are presented as a function of the elastic anisotropy factor in Sec. III in a form easily comparable with experiment. The results are discussed in Sec. IV.

II. PHONON FOCUSING EFFECTS OF ELASTIC ANISOTROPY ON PHASE- AND GROUP-VELOCITY DIRECTIONS IN SYMMETRY PLANES

The elastic properties of a cubic crystal can be characterized in terms of the second-order elastic

constants, C_{11}, C_{44}, and C_{12}. Maris[10] has shown that the phonon-focusing properties of elastically anisotropic crystals can be determined from the elastic ratios C_{12}/C_{11} and C_{44}/C_{11}. A representative sample of elastic solids with widely differing elastic ratios are shown in Fig. 1. The anisotropy factor A, is defined as

$$A = 2C_{44}/(C_{11}-C_{12}) \tag{1}$$

and is unity for elastically isotropic crystals.

In an elastically anisotropic crystal the phonon phase-velocity surfaces are nonspherical (see Table I) so that the phase and group velocities are collinear only along certain directions. The angular deviation between the phase- and group-velocity directions depends upon the polarization, the elastic anisotropy, and the direction of the wave vector. This is clearly illustrated for wave vectors restricted to the {100} and {110} symmetry planes of a cubic crystal in Figs. 2–6. If the wave vectors are confined to a particular symmetry plane, then by symmetry the corresponding group-velocity vectors are restricted to that same symmetry plane. The symmetry plane in this case is said to be cusp-free if $d\theta_k/d\theta_v > 0$, and exhibits cusp-free phonon focusing wherever $d\theta_k/d\theta_v > 1$.[20] Cuspidal onset in a symmetry plane (i.e., $d\theta_v/d\theta_k = 0$ at $\theta_v = \theta_k$) is thus associated with very high focusing about $\theta_v = \theta_k$. High focusing is also associated with cuspidal extrema where $|d\theta_v/d\theta_k| \ll 1$. Conditions for cusp-free phonon focusing for wave vectors in symmetry planes have been derived by Winternheimer *et al.*[20] Conditions for cuspidal onset have been derived by Musgrave,[36,37] Maris,[10] and Winternheimer *et al.*,[20] and are plotted as curves $C1$ through $C5$ in Fig. 1. Cuspidal onset can occur about the ⟨100⟩ directions in both the {100} and {110} planes (curves $C3$ and $C4$, respectively), about the ⟨110⟩ directions in both the {100} and {110} planes (curves $C2$ and $C5$, respectively), or about a direction ⟨θ_s⟩ with respect to the ⟨100⟩ axis in the {110} plane (curve $C1$). Angle θ_s is given by

$$\tan\theta_s = [2(C_{11}+C_{12})/(C_{11}+3C_{12}+2C_{44})]^{1/2} \tag{2}$$

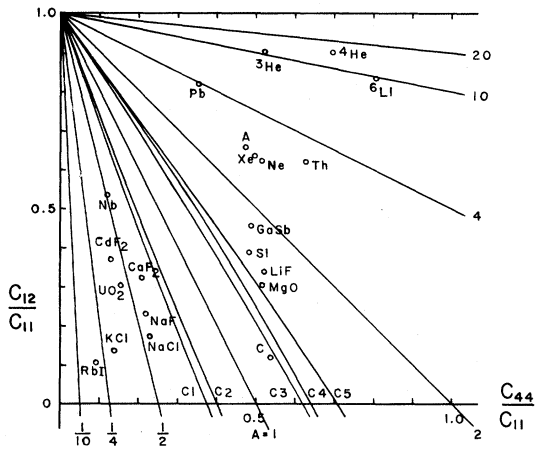

FIG. 1. Representative sample of elastic solids with widely differing elastic ratios C_{12}/C_{11} and C_{44}/C_{11}. The slightly curved loci, $C1-C5$, are conditions for cuspidal onset about collinear directions in the {110} and {100} symmetry planes. They are defined as follows: $C1$ is cuspidal onset about a direction, ⟨θ_s⟩, with respect to the ⟨100⟩ axis in the {110} plane; $C2$, cuspidal onset about the ⟨110⟩ direction in the {100} plane; $C3$ cuspidal onset about the ⟨100⟩ axis in the {100} plane; $C4$, cuspidal onset about the ⟨100⟩ axis in the {110} plane; $C5$, cuspidal onset about the ⟨110⟩ axis in the {110} plane. The straight A lines are labeled according to their anisotropy factor.

and is usually not far from the ⟨111⟩ direction. Cuspidal features in the group-velocity surface for the longitudinal mode are nonexistent.[20,36–39]

Note that for $A \neq 1$, the two transverse modes have different phase velocities along the ⟨110⟩ axis (Table I) so that this direction can be used to identify the two phase-velocity surfaces. For convenience in this paper, the phase-velocity surface having $\rho s^2 = (C_{11}-C_{12})/2$ along the ⟨110⟩ axis is designated $S1$; the surface having $\rho s^2 = C_{44}$ along the ⟨110⟩ axis, designated $S2$. If $A < 1$, surface $S1$ has the smaller transverse phase velocity in the {110} plane between the ⟨100⟩ and ⟨111⟩ directions, and the larger velocity in the {110} plane between the ⟨111⟩ and ⟨110⟩ directions. The converse is true in the {110} plane for $A > 1$. The

TABLE I. Values of ρs^2 for the longitudinal (L) and the two transverse (T) modes for the principal directions in cubic crystals in terms of the second-order elastic constants.

Axis	ρs_L^2	ρs_T^2	ρs_T^2
⟨100⟩	C_{11}	C_{44}	C_{44}
⟨110⟩	$(C_{11}+C_{12})/2+C_{44}$	C_{44}	$(C_{11}-C_{12})/2$
⟨111⟩	$(C_{11}+2C_{12}+4C_{44})/3$	$(C_{11}-C_{12}+C_{44})/3$	$(C_{11}-C_{12}+C_{44})/3$

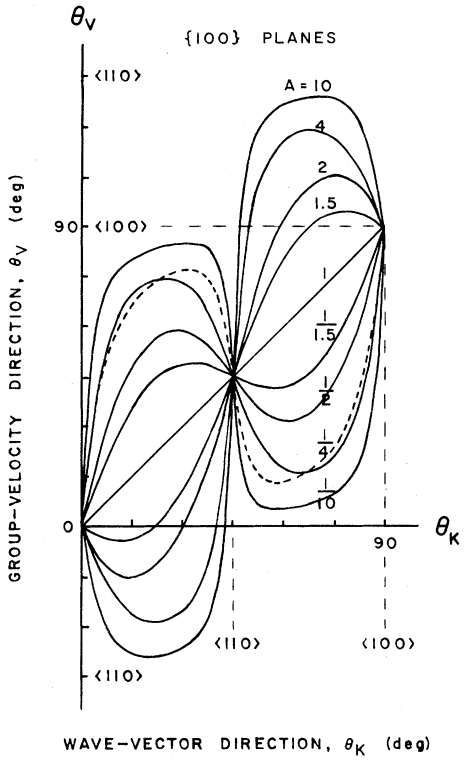

FIG. 2. Relation between the direction of the wave vector and the group-velocity vector in the {100} symmetry plane for the two transverse modes. The collinear, straight-line relation applies to the phase-velocity surface, designated $S2$ in the text, and is independent of the anisotropy factor A. The relation for surface $S1$ depends not only upon the anisotropy factor, but also upon the elastic ratio C_{12}/C_{11}. Note the pronounced cuspidal features about the ⟨110⟩ axis for $A < 1/1.5$, and about the ⟨100⟩ axis for $A > 1.5$ not exhibited for this surface in Fig. 4. Values of C_{12}/C_{11} are 0.1 for $A=0.1$ and 0.25 (dotted locus), 0.5 for $A=0.25-2$, and 0.9 for $A=4$ and 10.

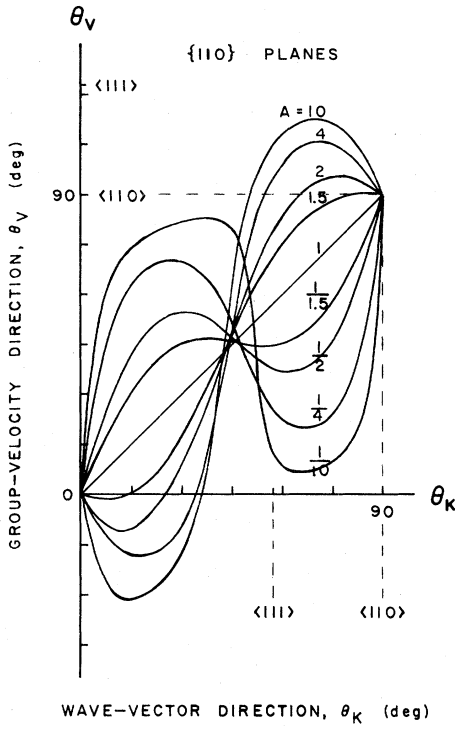

FIG. 3. Relation between the direction of the wave vector and the group-velocity vector in the {110} symmetry plane for the transverse surface designated $S2$ in the text. The relation is dependent not only upon the anisotropy factor but also upon C_{12}/C_{11}. Note the pronounced cuspidal features about the ⟨110⟩ axis for $A > 2$ not exhibited for this surface in Fig. 2. Note also the pronounced cusps near the ⟨111⟩ direction for $A < 0.5$. Values of C_{12}/C_{11} are 0.1 for $A=0.1$, 0.5 for $A=0.25-2$, and 0.9 for $A=4$ and 10.

cusps about the ⟨100⟩ and ⟨110⟩ axis in the {100} plane are associated with the phase-velocity surface $S1$; the cusps about the ⟨100⟩, ⟨110⟩, and ⟨θ_s⟩ directions in the {110} plane are associated with the surface $S2$.

Narrow cuspidal edges about the ⟨100⟩ axes exhibit fourfold symmetry, are localized and give a high phonon intensity along the ⟨100⟩ directions. Narrow cuspidal edges about the ⟨110⟩ axes, however, exhibit twofold symmetry and give sharp, knife-like ridges of phonon intensity along a wide angle in either the {110} or {100} planes, depending upon the elastic anisotropy.[13] For $A > 1$, these long ridges occur in the {100} planes, but for $A < 1$, they occur in the {110} planes. This is illustrated for an isotropic distribution of wave vectors such as that emitted by an ideal heat source in silicon and calcium fluoride, Figs. 7 and 8, respectively.[13] In both figures the heavy dark areas are bounded by cuspidal edges in the transverse group-velocity surfaces giving rise to strong phonon intensities. The cuspidal features for $A > 1$ about the ⟨110⟩ axis are associated with surface $S2$, and extend over a wide angle in the {100} plane. These cuspidal surfaces are generated by wave vectors which lie near, but straddle both sides of the {100} plane, and thus are not displayed when wave vectors are restricted to {100} planes. Conversely, the cuspidal features about the ⟨110⟩ axis associated with $S1$ and which, for $A < 1$, extend over a wide angle in the {110} plane are not displayed by wave vectors restricted to {110}

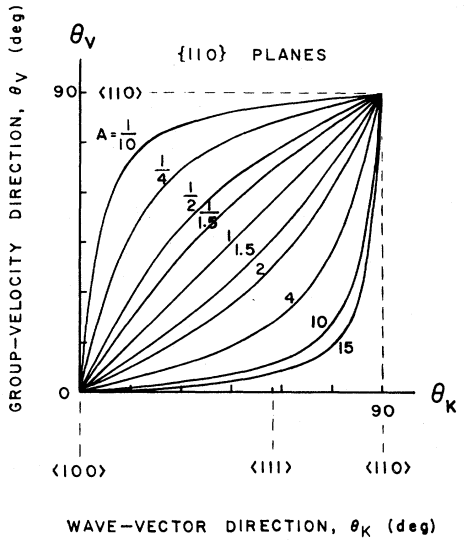

FIG. 4. Relation between the direction of the wave vector and the group-velocity vector in the {110} symmetry plane for the transverse surface designated $S1$ in the text. Note that the relation is independent of C_{12}/C_{11}. Note also that no cuspidal features are displayed because wave vectors are confined to the {110} plane.

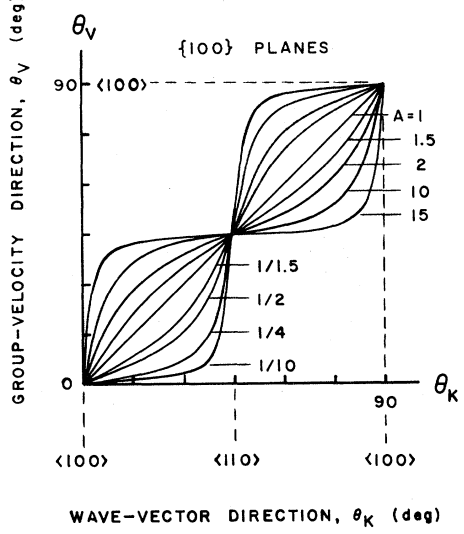

FIG. 5. Relation between the direction of the wave vector and the group-velocity vector in the {100} symmetry plane for the longitudinal mode. The relation is dependent not only upon the anisotropy factor but also upon C_{12}/C_{11}. Values of C_{12}/C_{11} are 0.1 for $A=0.1-1$, 0.5 for $A=1.5$ and 2, and 0.9 for $A=10$ and 15.

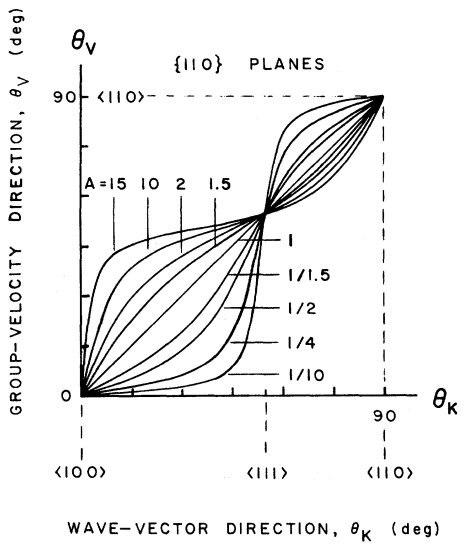

FIG. 6. Relation between the direction of the wave vector and the group-velocity vector in the {110} symmetry plane for the longitudinal mode. The relation is dependent not only upon the anisotropy factor but also upon C_{12}/C_{11}. Values of C_{12}/C_{11} are 0.1 for $A=0.1-1$, 0.5 for $A=1.5$ and 2, and 0.9 for $A=10$ and 15.

planes (Fig. 4). The high-phonon intensities resulting from conditions near cuspidal onset about the ⟨110⟩ axis in the {100} plane are illustrated for the (a) slower, (b) faster transverse modes in Figs. 9(a) and 9(b). Note, however, that the cuspidal onset is associated with surface $S1$ and gives rise to high intensities in the {110} planes. Since these planes intersect along the ⟨111⟩ axes, an enhanced phonon intensity occurs along these directions. A brief qualitative description of phonon focusing for each of the phase-velocity surfaces follows.

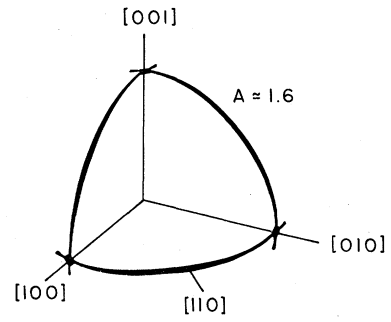

FIG. 7. Simplified schematic diagram illustrating phonon focusing for the two transverse modes of a cubic crystal with the elastic anisotropy factor A of silicon. Directions of high-phonon intensity are given by constructing lines from the origin to the heavy dark areas.

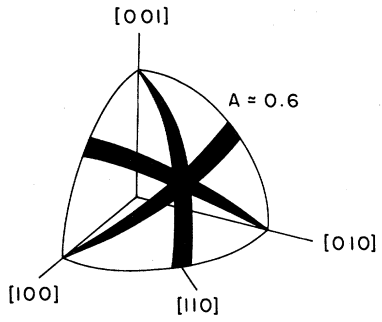

FIG. 8. Simplified schematic diagram illustrating phonon focusing for the two transverse modes of a cubic crystal with the elastic anisotropy factor of calcium fluoride. Directions of high-phonon intensity are given by constructing lines from the origin to the heavy dark areas.

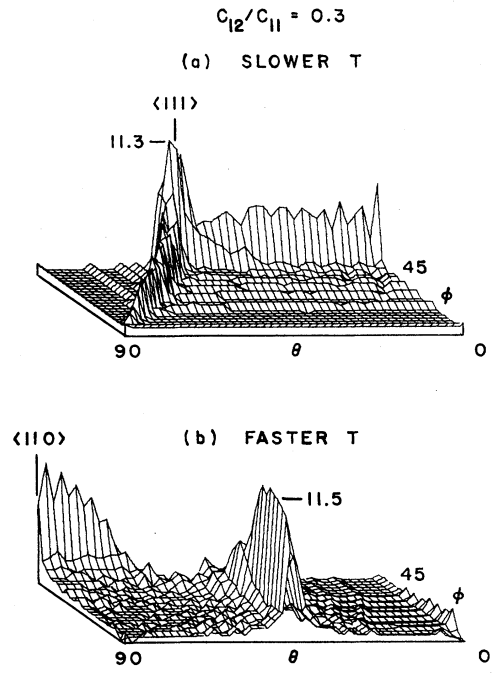

FIG. 9. Computer plotted profiles of phonon intensity near cuspidal condition $C2$ for transverse waves having (a) slower and (b) faster phase velocities, respectively. Since θ and ϕ are the spherical polar angles the $\langle 100 \rangle$ directions occur at $\theta=0$, $0 \leq \phi \leq 45$, and $\theta=90$, $\phi=0$; the $\langle 110 \rangle$ directions at $\theta=45$, $\phi=0$, and $\theta=90$, $\phi=45$; the $\langle 111 \rangle$ directions at $\theta=54.74$, $\phi=45$. The sharp ridges of high intensity arise from cuspidal onset of surface $S1$ about the $\langle 110 \rangle$ axes. Note that the high ridges appearing in $\{110\}$ planes, (b), continue in (a) to the $\langle 100 \rangle$ axes. The serrated appearance of the ridges is due to the coarse 1° mesh used in $\vec{k}$ space to generate the group-velocity distribution and the coarser 2° increment to the plotter.

A. Transverse waves

1. *Surface S1*

Note that for $A > 1$, focusing occurs about the $\langle 100 \rangle$ axis in the $\{110\}$ plane (Fig. 4). The strongest focusing about the $\langle 100 \rangle$ axis occurs in the $\{100\}$ plane (Fig. 2) for cuspidal onset condition $C3$. Defocusing occurs for $A > 1$, however, in the $\{100\}$ and $\{110\}$ planes along the $\langle 110 \rangle$ direction. For $A < 1$, focusing occurs about the $\langle 110 \rangle$ direction in the $\{110\}$ plane (Fig. 4). The strongest focusing about the $\langle 110 \rangle$ axis occurs in the $\{100\}$ plane (Fig. 2) for cuspidal condition $C2$. Defocusing, however, occurs for $A < 1$ about the $\langle 100 \rangle$ direction in the $\{100\}$ and $\{110\}$ planes.

2. *Surface S2*

Since the group and phase velocities are collinear in the $\{100\}$ plane, the strongest focusing about the $\langle 100 \rangle$ axis occurs in the $\{110\}$ plane (Fig. 3) for cuspidal condition $C4$. Similarly, the strongest focusing about the $\langle 110 \rangle$ axis occurs in the $\{110\}$ plane for cuspidal condition $C5$. For $A < 1$, however, strong defocusing occurs in the $\{110\}$ plane about the $\langle 100 \rangle$ and $\langle 110 \rangle$ directions (Fig. 3). In this case the strongest focusing occurs in the $\{110\}$ plane about the $\langle \theta_s \rangle$ axis for cuspidal condition $C1$.

B. Longitudinal waves

For small A, the focusing occurs about the $\langle 100 \rangle$ axis in the $\{100\}$ and $\{110\}$ planes, Figs. 5 and 6, respectively. For large A, the focusing occurs about the $\langle 111 \rangle$ directions (Fig. 6). Focusing about the $\langle 110 \rangle$ direction, however, depends upon the relative strengths of the focusing and defocusing ocurring in the two intersecting symmetry planes, respectively. For large A, the focusing occurring in $\{100\}$ planes (Fig. 5) is stronger than the defocusing in $\{110\}$ planes (Fig. 6) so that a net enhancement of longitudinal phonons results about the $\langle 110 \rangle$ direction. For small A, however, the defocusing in $\{100\}$ planes is stronger than the focusing in $\{110\}$ planes and a net depletion of longitudinal phonons occurs about the $\langle 110 \rangle$ direction.

III. CALCULATIONS OF EFFECTIVE PHONON MEAN FREE PATH, EFFECTIVE VELOCITY, SPECIFIC HEAT, AND PHONON CONDUCTIVITY

Calculations of the boundary-scattered phonon mean free path Λ_{eff} for cubic crystals as a function

of the elastic anisotropy factor A are performed using Eq. (3):

$$\Lambda_{\text{eff}}=3\kappa/(C_v v_{\text{eff}}) . \tag{3}$$

κ is the end-corrected thermal conductivity for samples of square cross section with side dimension D and thermal length L,[13,14] and C_v is the specific heat per unit volume. The thermal length of the sample is defined as the length of the thermal gradient produced along the heat-flow axis in a conventional thermal conductivity measurement,[13,14] and thus is usually less than the overall length of the sample.[40] The effective velocity v_{eff} is defined as

$$v_{\text{eff}}=\sum_{j=1}^{3}\langle\,|v_j|s_j^{-3}\rangle/\langle s_j^{-3}\rangle , \tag{4}$$

where $\langle\,|v_j|s_j^{-3}\rangle$ is the direction average of the phonon group velocity times the inverse cube phase velocity for polarization j. The Casimir velocity v_C is defined as

$$v_C=\sum_{j=1}^{3}\langle s_j^{-2}\rangle/\langle s_j^{-3}\rangle \tag{5}$$

and is smaller than v_{eff} except for elastically isotropic crystals. Dimensionless values of Λ_{eff}/D for samples of square cross section are plotted in Figs. 10–18.

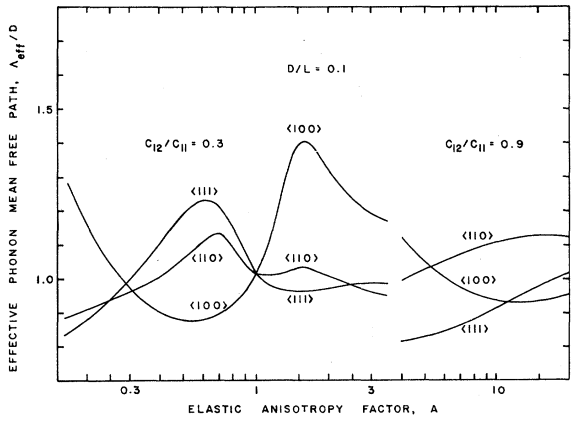

FIG. 10. Dimensionless boundary-scattered phonon mean free path Λ_{eff}/D for cubic crystals as a function of the elastic anisotropy factor A for heat-flow axis along principal directions. Calculations apply to samples of square cross section with side dimension D, thermal length L, and D/L of 0.10. The value of C_{12}/C_{11} was 0.3 for $A \leq 4$ and 0.9 for $A \geq 4$. Side-face orientations are {100} for the ⟨100⟩, {110} and {100} for the ⟨110⟩, and {110} and {112} for the ⟨111⟩ heat-flow axes.

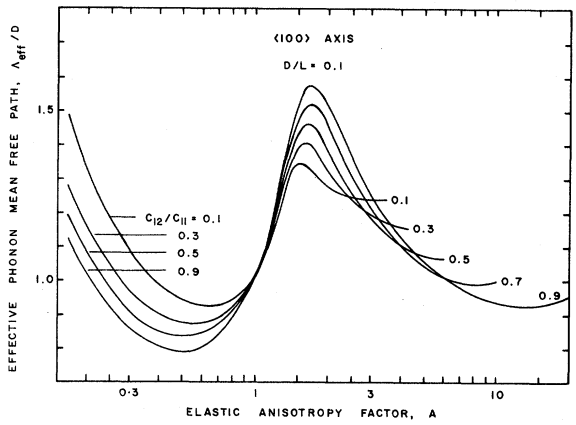

FIG. 11. Dimensionless boundary-scattered phonon mean free path Λ_{eff}/D for the ⟨100⟩ heat-flow axis as a function of the elastic anisotropy factor A and the ratio C_{12}/C_{11}. Calculations apply to samples of square cross section with D/L of 0.10. Side faces are oriented in {100} planes.

Calculations of the specific heat C_v and effective phonon velocity v_{eff} as a function of the elastic anisotropy factor A are given in Figs. 19 and 20, respectively. Results are displayed in dimensionless units as $C_v/\langle C_v\rangle$ and $v_{\text{eff}}/\langle v_C\rangle$, respectively, where $\langle C_v\rangle$ and $\langle v_C\rangle$ are the specific heat and Casimir velocity, respectively, calculated using the phase velocities along only the three principal axes of the crystal. The specific heat is given by

$$C_v=(2\pi^2/15)k_B(k_BT/\hbar)^3\sum_{j=1}^{3}\langle s_j^{-3}\rangle , \tag{6}$$

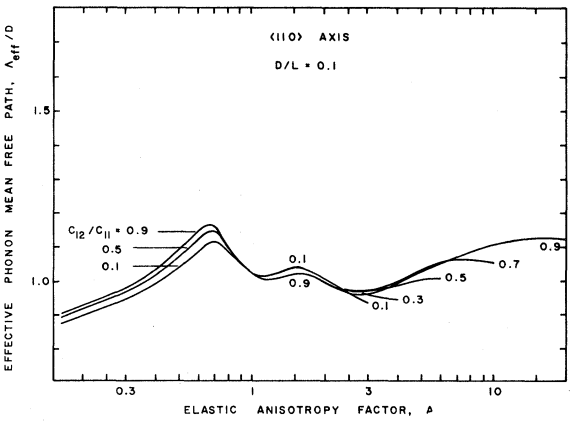

FIG. 12. Dimensionless boundary-scattered phonon mean free path Λ_{eff}/D for the ⟨110⟩ heat-flow axis as a function of the elastic anisotropy factor A and the ratio C_{12}/C_{11}. Calculations apply to samples of square cross section with D/L of 0.10. Side faces are oriented in {110} and {100} planes.

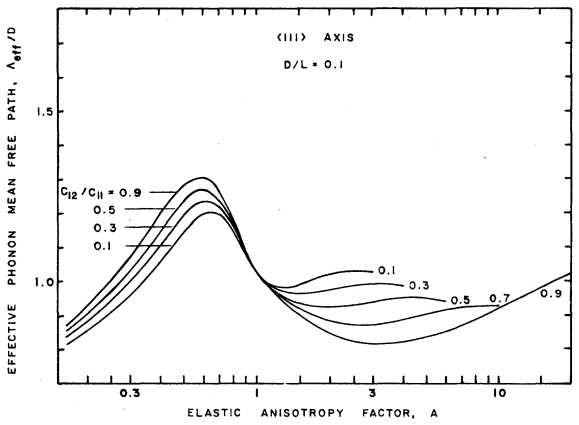

FIG. 13. Dimensionless boundary-scattered phonon mean free path Λ_{eff}/D for the ⟨111⟩ heat-flow axis as a function of the elastic anisotropy factor A and the ratio C_{12}/C_{11}. Calculations apply to samples of square cross section with D/L of 0.10. Side faces are oriented in {110} and {112} planes.

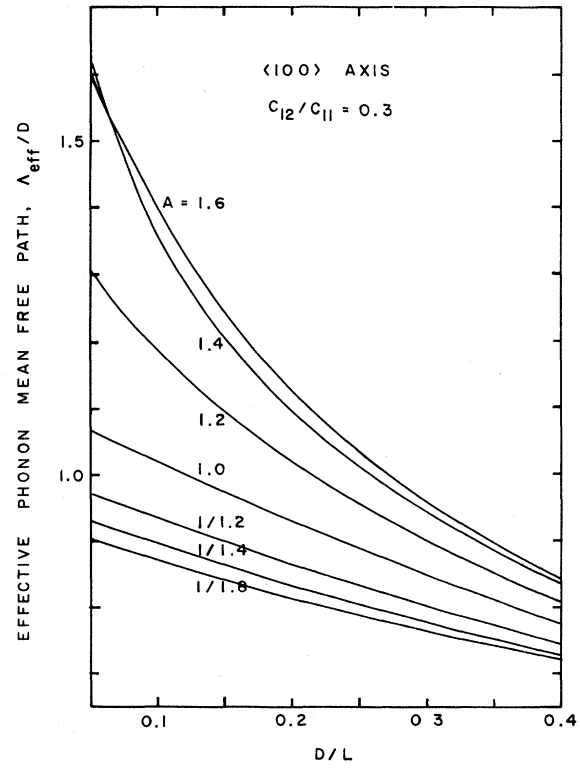

FIG. 14. Dimensionless phonon mean free path Λ_{eff}/D for the ⟨100⟩ heat-flow axis as a function of D/L and the elastic anisotropy factor, A. Calculations apply to samples of square cross section with side dimension D, thermal length L, and {100} side faces.

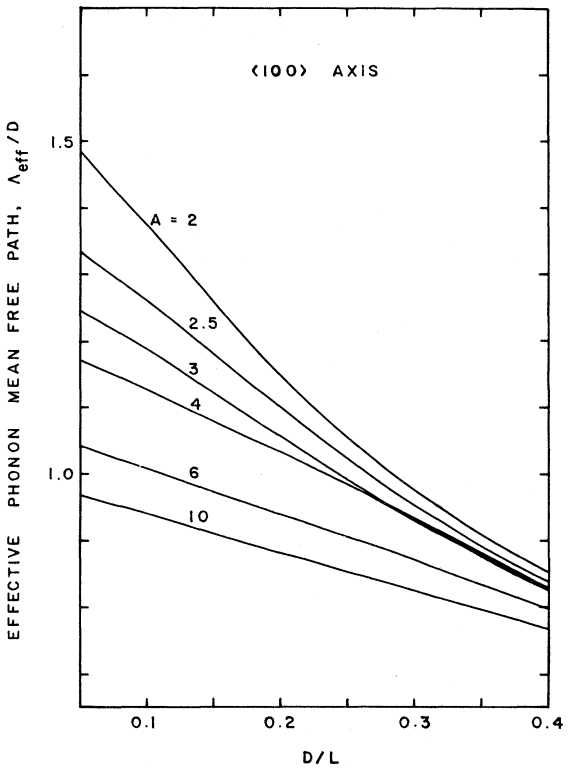

FIG. 15. Dimensionless phonon mean free path Λ_{eff}/D for the ⟨100⟩ heat-flow axis as a function of D/L and the elastic anisotropy factor A. The value of C_{12}/C_{11} was 0.5 for $A=2$, 2.5, and 3, and 0.9 for $A=4$, 6, and 10. Calculations apply to samples of square cross section with side dimension D, thermal length L, and {100} side faces.

where $(2\pi^2/15)k_B(k_B/\hbar)^3$ is equal to 40.77 GJ K^{-4}s^{-3}. Thus

$$C_v/\langle C_v\rangle = \sum_{j=1}^{3} \langle s_j^{-3}\rangle/\langle s_j^{-3}\rangle_3 , \tag{7}$$

and

$$\langle v_C\rangle = \sum_{j=1}^{3} \langle s_j^{-2}\rangle_3/\langle s_j^{-3}\rangle_3 , \tag{8}$$

where $\langle s_j^{-2}\rangle_3$ and $\langle s_j^{-3}\rangle_3$ denote the arithmetic averages over the ⟨100⟩, ⟨110⟩, and ⟨111⟩ directions of the inverse square and inverse cube phase velocity, respectively, for mode j. Expressions for ρs^2, where ρ is the density, are given for the three principal axes of the cubic lattice in Table I.

Calculations of κ for samples of square cross section are given in Figs. 21–23. Values of κ for silicon and calcium fluoride samples of rectangular cross section and varying side-face-width ratio are given in Figs. 24 and 25, respectively. These re-

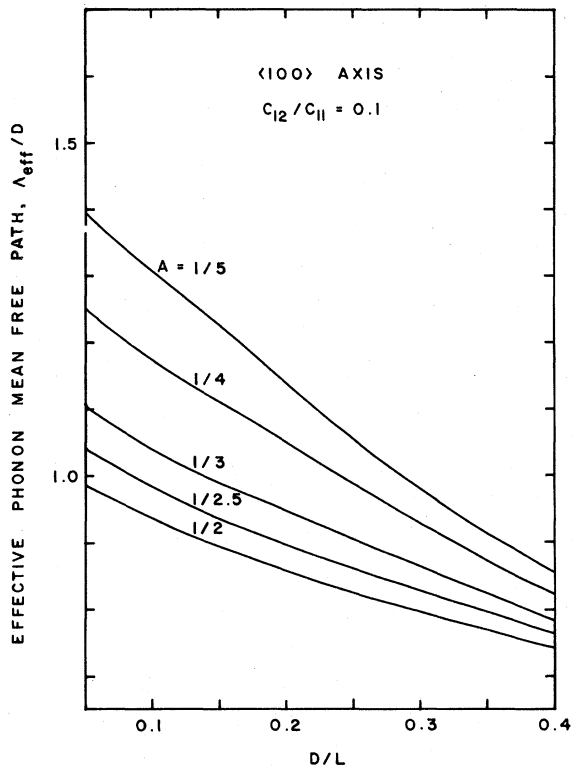

FIG. 16. Dimensionless phonon mean free path Λ_{eff}/D for the ⟨100⟩ heat-flow axis as a function of D/L and the elastic anisotropy factor A. Calculations apply to samples of square cross section with side dimension D, thermal length L, and {100} side faces.

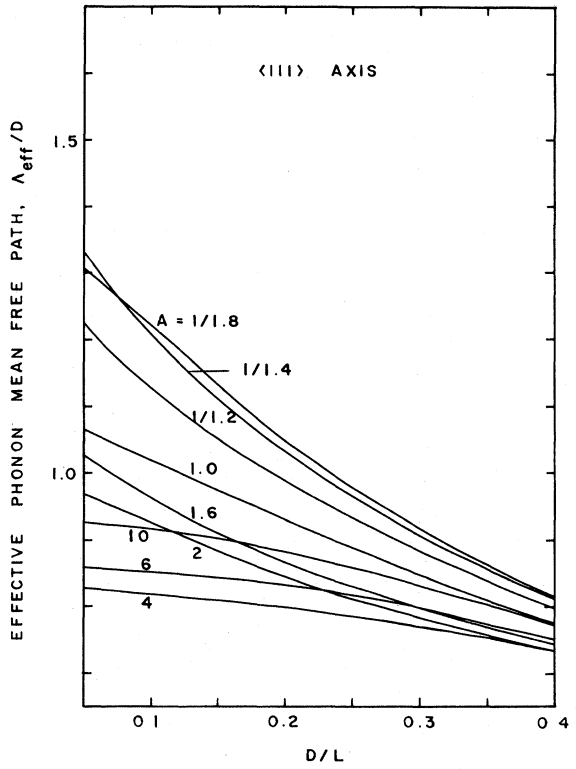

FIG. 17. Dimensionless phonon mean free path Λ_{eff}/D for the ⟨111⟩ heat-flow axis as a function of D/L and the elastic anisotropy factor A. The value of C_{12}/C_{11} was 0.3 for $A=1/1.8$, 1/1.4, 1/1.2, 1, and 1.6; 0.5 for $A=2$; and 0.9 for $A=4$, 6, and 10. Calculations apply to samples of square cross sections with side dimension D and thermal length L. Side faces are oriented in {110} and {112} planes. The reversed trend for $A=4$, 6, and 10 is also evident in Figs. 13 and 23.

sults are expressed in dimensionless units as $\kappa/\langle\kappa_C\rangle$, where $\langle\kappa_C\rangle$ is the Casimir thermal conductivity for infintely long, elastically anisotropic crystals defined here as

$$\langle\kappa_C\rangle=\tfrac{1}{3}\langle C_v\rangle\langle v_C\rangle\Lambda_C\ . \tag{9}$$

$\langle C_v\rangle$ and $\langle v_C\rangle$ are the approximate specific heat and Casimir velocity, respectively, for elastically anisotropic crystals given in Eqs. (7) and (8), and Λ_C is the Casimir length for rods of infinite thermal length. For rods of circular cross section with diameter D

$$\Lambda_C=D\ , \tag{10}$$

but for rods of rectangular cross section with side-face-width ratio n and sides $D_1=nD$ and $D_2=D$[13,14]

$$\begin{aligned}\Lambda_C=(n^{1/2}D/4)\{&3n^{1/2}\ln[n^{-1}+(n^{-2}+1)^{1/2}]\\&+3n^{-1/2}\ln[n+(n^2+1)^{1/2}]\\&-(n+n^3)^{1/2}+n^{3/2}\\&-(n^{-1}+n^{-3})^{1/2}+n^{-3/2}\}\ .\end{aligned} \tag{11}$$

For rods of square section Eq. (11) reduces to

$$\Lambda_C=1.115D\ . \tag{12}$$

For elastically isotropic crystals $A=1$, and the end-corrected thermal conductivity $\kappa/\langle\kappa_C\rangle=0.915$ for $D/L=0.1$

Calculations of κ were performed with double precision on a digital computer using Casimir's theory generalized for end effects and phonon focusing.[13,14] The details are essentially the same as those already described elsewhere.[13] Phase and group velocities for each mode were calculated for a large number of different wave-vector directions $\vec{k}$ in a hemisphere, the polar axis being parallel to the heat-flow ⟨100⟩ axis of the sample and the side faces oriented in {100} planes. Results for heat flow along the ⟨110⟩ and ⟨111⟩ directions were obtained by coordinate rotations so that one

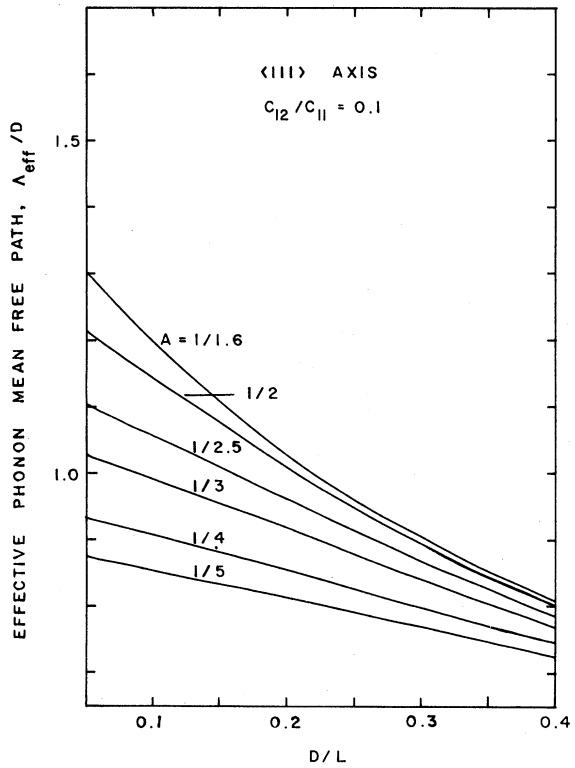

FIG. 18. Dimensionless phonon mean free path Λ_{eff}/D for the ⟨111⟩ heat-flow axis as a function of D/L and the elastic anisotropy factor A. Calculations apply to samples of square cross section with side dimension D and thermal length L. Side faces are oriented in {110} and {112} planes.

side face, respectively, was oriented in the {110} plane. The numerical integration over all $\vec{k}$ required to obtain the thermal conductivity was performed using a uniform density of wave vectors. The number of $\vec{k}$ vectors per unit solid angle was maintained nearly constant over the entire hemisphere by increasing the azimuthal mesh size $\Delta\phi$ while decreasing the polar angle θ. The mesh size $\Delta\theta$ was $\frac{1}{2}\pi/n$, where n is an integer, and the mesh size $\Delta\phi$ was $2\pi/m$, where m is the nearest integer to $4n\sin\theta$. The direction of the wave vector was scanned over ϕ and θ, respectively, from initial angles (θ_i,ϕ_i) given by

$$\theta_i=\pi/2-\Delta\theta/2\,, \tag{13}$$

$$\phi_i=\Delta\theta/2\,. \tag{14}$$

A small multiplicative correction, $(4n/m)\sin\theta$, was applied to the partial summation in each full scan over ϕ at constant θ before changing to a new value of θ. This helped to eliminate any effects arising from the slight nonuniformity of wave-vector density. This correction though most significant near the pole made little difference, however, in the final results.

Preliminary calculations of phonon conductivity were performed for $D/L=0.1$ using a mesh size $\Delta\theta$ of 3° with 2292 different directions in $\vec{k}$ space. Accuracy was checked by making spot checks and using a progressively finer mesh. For $4\leq A<9$ a maximum mesh size of 1° was found necessary to obtain values for the ⟨100⟩ axis with less than 0.5% error. For $A<0.8$, however, the strong defocusing properties of both transverse waves about the ⟨100⟩ axis required progressively smaller mesh sizes as A decreased before ⟨100⟩ results converged to a reliable value. For $A=\frac{1}{6}$ and $D/L=0.10$ a mesh size of 0.5° with 82 508 different $\vec{k}$ directions was required before results for the ⟨100⟩ axis converged with less than 0.5% error. As expected, results for the ⟨110⟩ and ⟨111⟩ axes were less sensitive to larger mesh sizes. End-correction calculations (Figs. 14–18) were performed using in each case one-half the corresponding mesh size used for $D/L=0.1$ and further served to check accuracy. Errors are believed to be less than 0.6% for $A>0.5$ with maximum errors at $A\leq 0.2$ of 1%. These results are thus more accurate than those reported previously.[21]

Calculations of phonon intensity in Fig. 9 were determined using a 1° mesh in the polar angles θ and ϕ, the number of wave vectors at each point weighted to give a uniform density. The intensities were calculated as the ratio of the number of group-velocity vectors to the number of wave vectors for a solid angle of four square degrees. Because of the fixed mesh in ϕ a much larger number of different azimuthal wave-vector directions occur about the ⟨100⟩ direction corresponding to $\theta=0$, $0\leq\phi\leq 45$ than about the ⟨100⟩ direction given by $\theta=90$, $\phi=0$. As a result, the ridge in the {110} plane near $\theta=90$, $\phi=0$ [Fig. 9(a)] lacks the sharp resolution and high amplitude of the one near $\theta=0$, $\phi=45$. The calculated intensities appear rather ragged and serrated for the two transverse modes because a coarse mesh of only four different wave-vector directions were used in each 2°×2° box.

Use of Figs. 19–23 and a hand calculator to determine $\langle C_v\rangle$, $\langle v_C\rangle$, and $\langle\kappa_C\rangle$ yields the correct specific heat, effective velocity, and phonon conductivity, respectively, for elastically anisotropic cubic crystals of square cross section and $D/L=0.10$. The correction to the phonon conductivity κ/T^3 for samples of square cross section

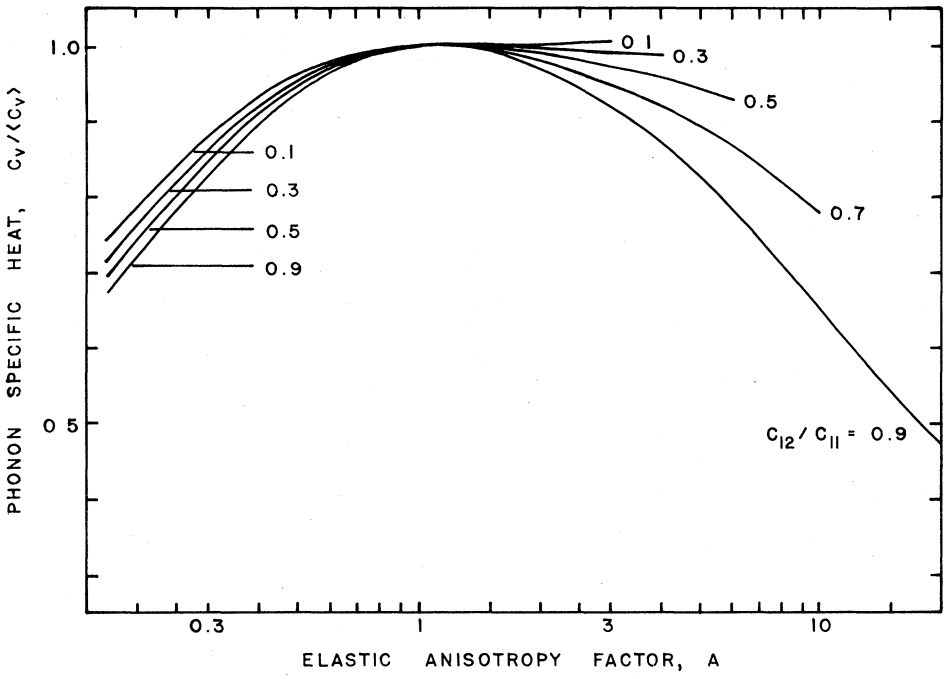

FIG. 19. Dimensionless specific heat $C_v/\langle C_v \rangle$ as a function of the elastic anisotropy factor A and the elastic constant ratio C_{12}/C_{11}. The approximate specific heat $\langle C_v \rangle$ is defined in the text.

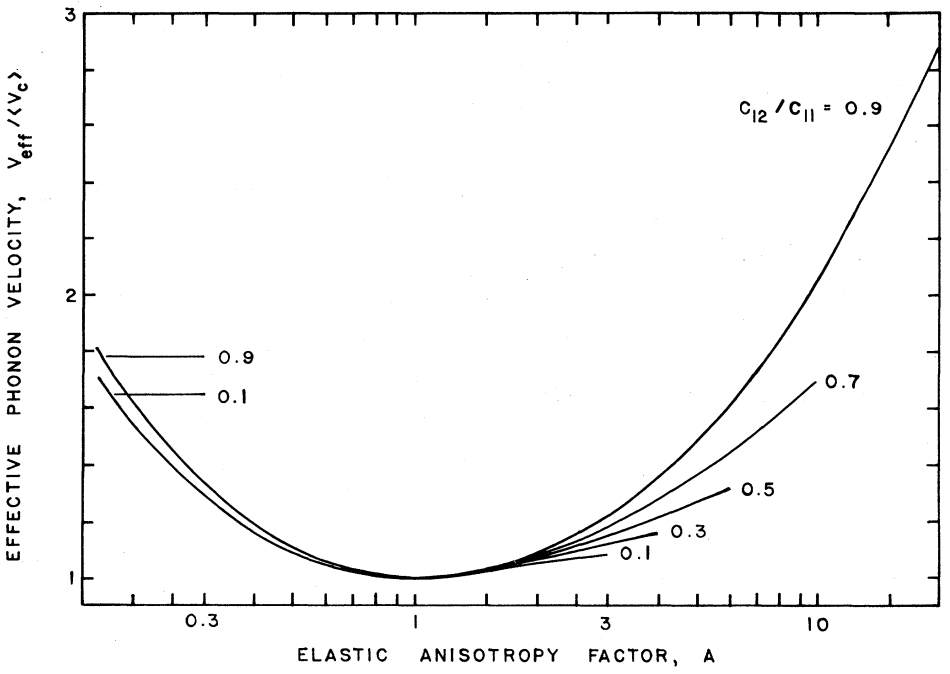

FIG. 20. Dimensionless effective phonon velocity $v_{eff}/\langle v_C \rangle$ as a function of the elastic anisotropy factor A and the elastic constant ratio C_{12}/C_{11}. The approximate Casimir velocity $\langle v_C \rangle$ is defined in the text.

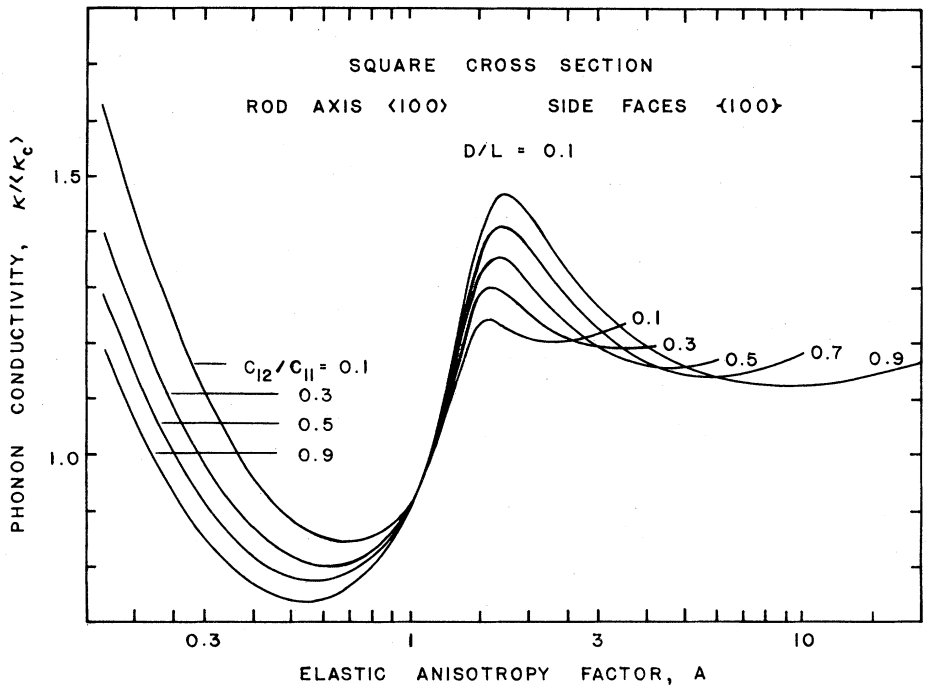

FIG. 21. Dimensionless boundary-scattered thermal conductivity $\kappa/\langle\kappa_C\rangle$ for the $\langle 100\rangle$ heat-flow axis as a function of the elastic anisotropy factor A and the elastic constant ratio C_{12}/C_{11}.

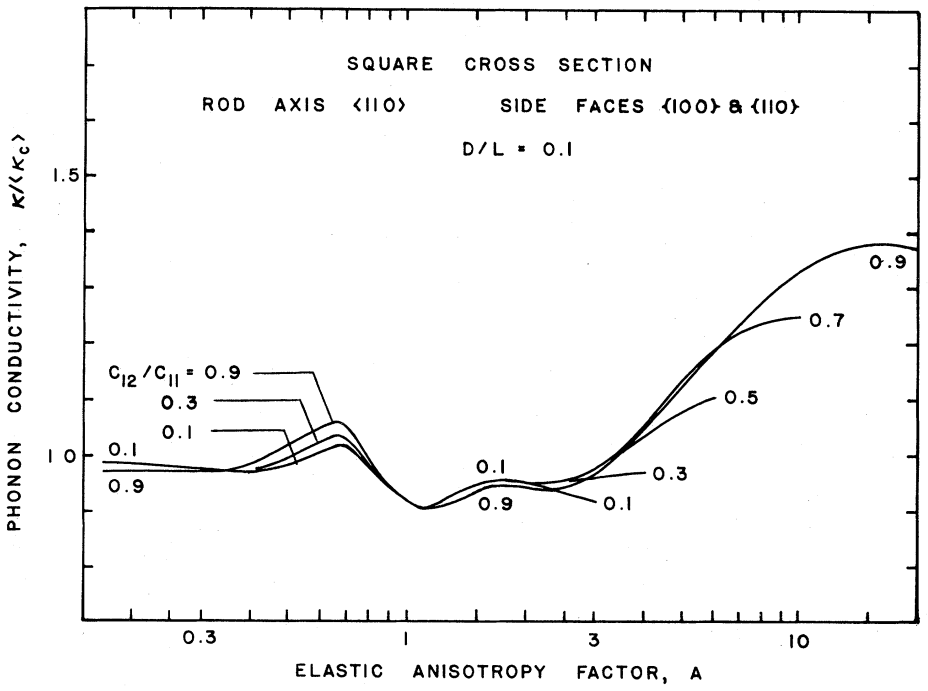

FIG. 22. Dimensionless boundary-scattered thermal conductivity $\kappa/\langle\kappa_C\rangle$ for the $\langle 110\rangle$ heat-flow axis as a function of the elastic anisotropy factor A and the elastic constant ratio C_{12}/C_{11}.

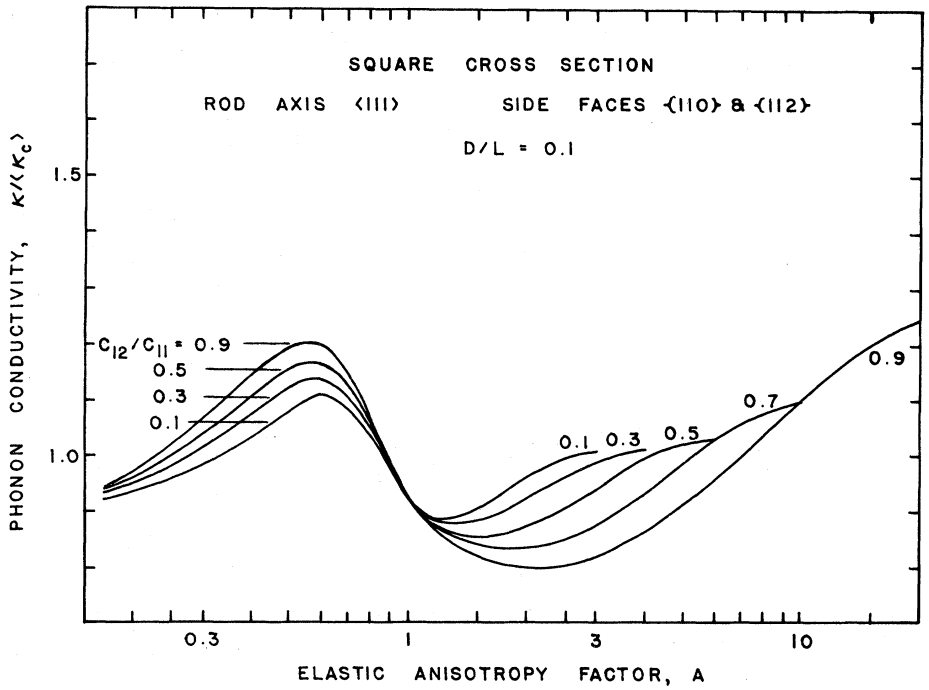

FIG. 23. Dimensionless boundary-scattered thermal conductivity $\kappa/\langle\kappa_C\rangle$ for the $\langle 111\rangle$ heat-flow axis as a function of the elastic anisotropy factor A and the elastic constant ratio C_{12}/C_{11}.

but different D/L can be obtained from Figs. 14–18. Values of κ/T^3 for silicon and calcium fluoride samples of rectangular cross section and $(D_1D_2)^{1/2}/L=0.10$ can be obtained from Figs. 24 and 25, respectively. Note that the thermal conductivity κ/T^3 depends only upon the linear dimensions D_1, D_2, and L the sample density ρ, and the second-order elastic constants. With the use of the supplied curves predictions of the boundary-scattered phonon conductivity should be possible with no more error than is presently realized in experimental measurements.

IV. DISCUSSION

Cubic crystals exhibit a wide range of elastic anisotropies. Materials that have similar coordinates C_{12}/C_{11} and C_{44}/C_{11} (Fig. 1) have similar phonon-focusing characteristics. Materials that have coordinates on opposite sides of the elastic anisotropy line, $A=1$, have contrasting properties. Note that as A increases ($A>1$), cusps in the group-velocity surface appear about the $\langle 100\rangle$ axis, first in the $\{100\}$ plane (curve $C3$), then in the $\{110\}$ plane (curve $C4$), and finally about the $\langle 110\rangle$ axis in the $\{110\}$ plane (curve $C5$). As A

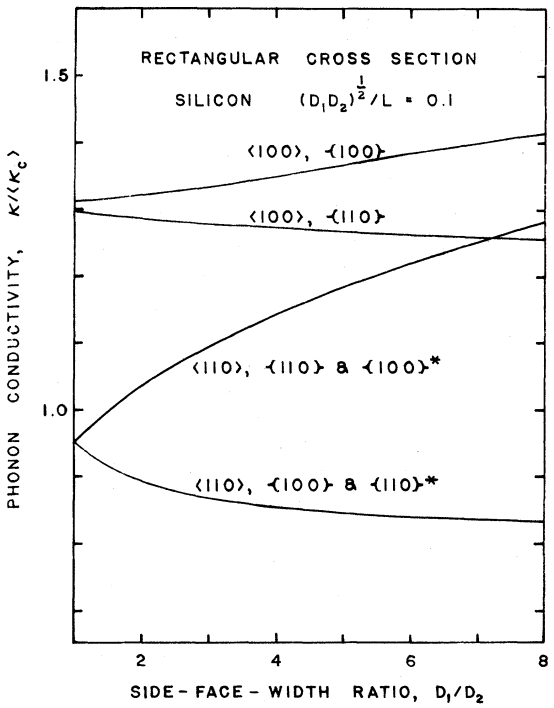

FIG. 24. Dimensionless boundary-scattered thermal conductivity $\kappa/\langle\kappa_C\rangle$ for $\langle 100\rangle$ and $\langle 110\rangle$ silicon rods of rectangular cross section and varying side-face-width ratio D_1/D_2, using the elastic constants of H. J. McSkimin and P. Andreatch [J. Appl. Phys. 35, 2161 (1964)]. The wider-side face is indicated by an asterisk.

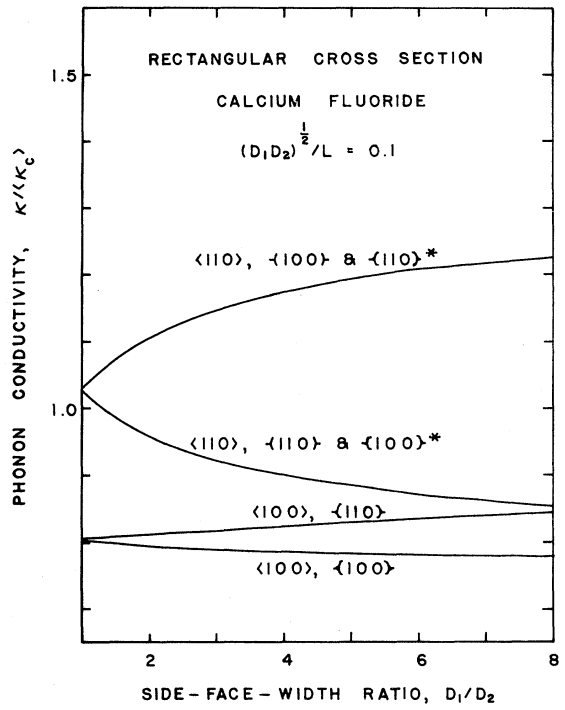

FIG. 25. Dimensionless boundary-scattered thermal conductivity $\kappa/\langle\kappa_C\rangle$ for ⟨100⟩ and ⟨110⟩ calcium fluoride rods of rectangular cross section and varying side-face-width ratio D_1/D_2 using the elastic constants of D. R. Huffmann and M. H. Norwood [Phys. Rev. 117, 709 (1960)]. The wider-side face is indicated by an asterisk.

decreases ($A<1$), however, cusps appear about the ⟨110⟩ axis in the {100} plane (curve $C2$), then about the $\langle\theta_s\rangle$ direction in the {110} plane (curve $C1$). In {100} planes cuspidal features in the group-velocity surface arise from surface $S1$ (Fig. 2), but in the {110} planes arise from surface $S2$ (Fig. 3).

Note that for further increases in A ($A>1.5$), the cusps that appear about the ⟨100⟩ axis (Figs. 2 and 3) and exhibit fourfold symmetry, and the cusps that appear about the ⟨110⟩ axis (Fig. 3) but exhibit twofold symmetry all increase dramatically in width. For $A=1.5$, $C_{12}/C_{11}=0.5$, for example, the cusp width about the ⟨100⟩ axis is 9° and 3° in the {100} and {110} planes, respectively, and the cusp width about the ⟨110⟩ axis in the {110} plane is 1°. For $A=4$, $C_{12}/C_{11}=0.9$, these cusps have widened to 57°, 38°, and 32°, respectively, and for $A=10$, $C_{12}/C_{11}=0.9$, to 78°, 63°, and 45°, respectively. As A decreases ($A<0.7$), it is the cusp widths about the ⟨110⟩ axis in the {100} plane and about the $\langle\theta_s\rangle$ direction in the {110} plane which increase dramatically. For $A=1/1.5$, $C_{12}/C_{11}=0.5$, the cusp width about the ⟨110⟩ axis in the {100} plane is 8°, and about the $\langle\theta_s\rangle$ axis in the {110} plane 2°. For $A=0.25$, $C_{12}/C_{11}=0.5$, these cusps have widened to 58° and 51°, respectively. The transverse intensities along collinear directions reach a maximum on cuspidal onset, then decrease as the cuspidal edges progressively widen (see Figs. 2 and 3). Strong defocusing can actually occur along these associated collinear directions for sufficiently widened cusps. Under these conditions the highest transverse intensities occur along the cuspidal extrema.

For elastically isotropic crystals, phonon focusing is absent and the only correction to the boundary-scattered mean free path Λ_{eff} and thermal conductivity κ is due to a finite thermal length. For a slight increase in the elastic anisotropy factor ($1.5>A>1$), however, there is a sharp rise in Λ_{eff} and κ along a ⟨100⟩ heat-flow axis as a result of phonon focusing (see Figs. 11 and 21). A decrease in A ($0.6<A<1$) decreases the heat flow along a ⟨100⟩ axis, but increases the conduction along a ⟨111⟩ rod axis (see Figs. 13 and 23). Silicon ($A=1.566$, $C_{12}/C_{11}=0.388$) is very near the maximum for ⟨100⟩ rods in Figs. 11 and 21, and near the minimum for ⟨111⟩ rods in Figs. 13 and 23. The enhanced thermal conductivity along the ⟨100⟩ axis is due to the strong focusing of transverse waves resulting from cuspidal edges about the ⟨100⟩ direction (Fig. 7). Similarly, the low thermal conductivity for ⟨111⟩ rods is due to the defocusing of phonons along the ⟨111⟩ directions. Calcium fluoride ($A=0.609$, $C_{12}/C_{11}=0.322$) is very near the maximum for ⟨111⟩ rods in Figs. 13 and 23, and near the minimum for ⟨100⟩ rods in Figs. 11 and 21. The enhanced conductivity along the ⟨111⟩ axis is due to the strong focusing about $\langle\theta_s\rangle$ and in the {110} planes that intersect along the ⟨111⟩ directions (Fig. 8). Similarly, the low conductivity for ⟨100⟩ rods is due to the lower phonon intensities along this axis. In retrospect, the elastic anisotropy factors for silicon and calcium fluoride were ideal for examining anisotropic heat conduction in the boundary-scattering region.

For larger values of A ($20>A>1.6$), an increase in A broadens the cusps about the ⟨100⟩ axes and about the {100} planes, decreasing the heat flow along the ⟨100⟩ rod axis. For large values of A, these cuspidal edges broaden toward the ⟨110⟩ directions and can contribute to increased heat flow along a ⟨110⟩ rod axis in shorter samples. Similarly, smaller values of A ($0.16<A<0.6$) broaden the cusps about the $\langle\theta_s\rangle$ axes and about

the {110} planes, decreasing the focusing and heat flow along the ⟨111⟩ rod axis. The broadening of these cuspidal surfaces toward the ⟨100⟩ directions can contribute to increased heat flow in shorter samples along the ⟨100⟩ rod axis. There is some evidence of this in Fig. 16.

Note also that for constant A an increase in C_{12}/C_{11} decreases C_{44}/C_{11} and thus increases the relative contribution of the slower modes to the heat flow. Since the slower modes are strongly focused, there is an increase in the thermal-conductivity maximum with C_{12}/C_{11} for ⟨100⟩ and ⟨111⟩ axis rods (see Figs. 21 and 23). Conversely, a decrease in C_{12}/C_{11} increases the relative contribution of longitudinal waves to the heat flow. For small A and C_{12}/C_{11}, there is strong focusing of longitudinal waves about the ⟨100⟩ axis. These two effects, at constant A, cause a rapid rise in thermal conductivity along a ⟨100⟩ heat-flow axis with a decrease in C_{12}/C_{11}. For constant C_{12}/C_{11} an increase in A increases C_{44}/C_{11} and thus increases the contribution of longitudinal waves to the flow of heat. For $A>4$, some focusing of longitudinal waves occurs about the ⟨110⟩ and ⟨111⟩ directions and is responsible for part of the increase in κ along these directions. The major contribution to the increase in $\kappa/\langle\kappa_C\rangle$, however, in Figs. 22 and 23 is due to corrections for $\langle C_v\rangle$ and $\langle v_C\rangle$ (Figs. 19 and 20), which become more significant for larger values of A.

Although there is some enhancement of the thermal conductivity along ⟨110⟩ heat-flow axes for silicon and calcium, the differences for samples of square cross section are relatively small (see Figs. 12 and 22). Phonon focusing occurs along the ⟨110⟩ directions in both silicon and calcium fluoride; for silicon the focusing is concentrated in {100} planes, for calcium fluoride in {110} planes. Greater anisotropies can be observed along ⟨110⟩ axes, however, for samples of rectangular cross section with different orientations of the wider-side face. Figure 7 shows that silicon samples with the same ⟨100⟩ or ⟨110⟩ rod axis should have greater conductivities when the wider-side face is oriented in the {100} plane (the plane of high phonon intensity) than in the {110} plane. This was indeed observed in our original measurements with ⟨110⟩ axis rods of silicon with rectangular cross section.[13,14] Conversely, Fig. 8 shows that calcium fluoride samples with the same ⟨100⟩ or ⟨110⟩ rod axis should have greater conductivities when the wider-side face is oriented in the {110} plane (the plane of high phonon intenisty) than in the {100} plane. Results for silicon are given in Fig. 24, and for calcium fluoride in Fig. 25. Both figures show that for samples of rectangular cross section with the same rod axis, higher conductivities are predicted when the wider-side face is oriented in the plane of high-phonon intensity, the amount of anisotropy depending on the rod axis and the width ratio of the side faces. The greatest differences occur for rods aligned along the ⟨110⟩ directions.

Note also that corrections for end effects (Figs. 14–18) depend particularly upon any focusing or defocusing along the sample rod axis. Longer samples have longer phonon flight paths to reach the end surfaces and thus have longer phonon mean free paths. Strong focusing (defocusing) along the rod axis therefore increases (decreases) the phonon mean free path and thus increases (decreases) the dependence of the thermal conductivity upon sample length. For very short samples effects of elastic anisotropy disappear and all rod-axis directions tend to have the same phonon mean free path and thermal conductivity.

ACKNOWLEDGMENTS

The author wishes to express his appreciation to the Worcester Area College Computation Center at Worcester Polytechnic Institute for the use of their computing facilities. Appreciation is also expressed to two of my former students: D. Z. Essagh for his help with computer work, and J. M. Kennedy for programming and operating the computer plotting subroutine.

[1] J. M. Ziman, *Electrons and Phonons* (Oxford University Press, London, 1960).
[2] P. Carruthers, Rev. Mod. Phys. 33, 92 (1961).
[3] P. G. Klemens, in *Solid State Physics*, edited by F. Seitz and D. Turnbull (Academic, New York, 1958), Vol. 7, p. 1.
[4] P. G. Klemens, in *Thermal Conductivity*, edited by R. P. Tye (Academic, New York, 1969), Vol. 1, p. 1.
[5] H. B. G. Casimir, Physica (Utrecht) 5, 495 (1938).
[6] R. Berman, F. E. Simon, and J. M. Ziman, Proc. R.

Soc. London Ser. A 220, 171 (1953).
[7]R. Berman, E. L. Foster, and J. M. Ziman, Proc. R. Soc. London Ser. A 231, 130 (1955).
[8]B. Taylor, H. J. Maris, and C. Elbaum, Phys. Rev. Lett. 23, 416 (1969).
[9]B. Taylor, H. J. Maris, and C. Elbaum, Phys. Rev. B 3, 1462 (1971).
[10]H. J. Maris, J. Acoust. Soc. Am. 50, 812 (1971).
[11]M. Lax and V. Narayanamurti, in *Phonon Scattering in Condensed Matter,* edited by H. J. Maris (Plenum, New York, 1980), p. 337; also Phys. Rev. B 22, 4876 (1980).
[12]P. Taborek and D. Goodstein, Phys. Rev. B 22, 1550 (1980).
[13]A. K. McCurdy, Ph.D. thesis, Brown University, 1971 (unpublished) (available from University Microfilms, Inc., Ann Arbor, Michigan, Order No. 72-12 047).
[14]A. K. McCurdy, H. J. Maris, and C. Elbaum, Phys. Rev. B 2, 4077 (1970).
[15]A. C. Anderson, M. E. Malinowski, Phys. Rev. B 5, 3199 (1972).
[16]J. W. Vandersande, Phys. Rev. B 13, 4560 (1976).
[17]J. W. Vandersande, J. Phys. (Paris) Colloq. C6, Suppl. 8, 39, C6-1017 (1978).
[18]C. G. Winternheimer and A. K. McCurdy, Solid State Commun. 14, 919 (1974).
[19]A. K. McCurdy, Phys. Rev. B 9, 466 (1974).
[20]C. G. Winternheimer and A. K. McCurdy, Phys. Rev. B 18, 6576 (1978).
[21]A. K. McCurdy, in *Phonon Scattering in Condensed Matter,* edited by H. J. Maris, (Plenum, New York, 1980), p. 341.
[22]F. Rösch and O. Weis, Z. Phys. B 25, 101 (1976).
[23]R. Rösch and O. Weis, Z. Phys. B 25, 115 (1976).
[24]J. Philip and K. S. Viswanathan, Phys. Rev. B 17, 4969 (1978).
[25]V. Narayanamurti and R. C. Dynes, Phys. Rev. B 12, 1731 (1975).
[26]P. Taborek and D. Goodstein, in *Phonon Scattering in Condensed Matter,* Ref. 21, p. 215.
[27]J. C. Hensel and R. C. Dynes, in *Phonon Scattering in Condensed Matter,* Ref. 21, p. 395.
[28]M. Greenstein and J. P. Wolfe, Phys. Rev. Lett. 41, 715 (1978).
[29]J. P. Wolfe, M. Greenstein, G. A. Northrop, and M. Tamor, in *Phonon Scattering in Condensed Matter,* Ref. 21, p. 377.
[30]G. A. Northrop and J. P. Wolfe, Phys. Rev. Lett. 43, 1424 (1979).
[31]G. A. Northrup and J. P. Wolfe, Phys. Rev. B 22, 6196 (1980).
[32]W. Eisenmenger, in *Phonon Scattering in Condensed Matter,* Ref. 21, p. 303.
[33]V. Narayanamurti, M. A. Chin, and R. A. Logan, in *Phonon Scattering in Condensed Matter,* Ref. 21, p. 429.
[34]Note that expressions for the amplification factor in the orthorhombic, tetragonal, and cubic lattices given in Tables III, IV, and V, respectively, of Ref. 20 are approximate, and are derived for those group-velocity surfaces which are free of cusps. Note also that the amplificiation factors for cubic crystals given in Table V, although in different algebraic form, nevertheless agree with those derived earlier in Ref. 10 by Maris.
[35]A. K. McCurdy (unpublished).
[36]M. J. P. Musgrave, Proc. Cambridge Philos. Soc. 53, 897 (1957).
[37]M. J. P. Musgrave, *Crystal Acoustics* (Holden-Day, San Francisco, 1970). Although out of print, this reference contains many diagrams of group-velocity surfaces for a number of different crystal symmetries.
[38]G. F. Miller and M. J. P. Musgrave, Proc. R. Soc. London Ser. A 236, 352 (1956).
[39]G. F. D. Duff, Philos. Trans. R. Soc. London 252, 249 (1960).
[40]The thermal length in our original experiments was the distance between the centers of the heat source and heat sink, respectively.